Wave Motion 51 (2014) 743–757

Contents lists available at ScienceDirect

Wave Motion

journal homepage: www.elsevier.com/locate/wavemoti

A rheological equation for anisotropic–anelastic media and simulation of field seismograms

Patricia M. Gauzellino [a,*], José M. Carcione [b], Juan E. Santos [c,d,e], Stefano Picotti [b]

[a] Departamento de Geofísica Aplicada, Fac. Ciencias Astronómicas y Geofísicas, UNLP, Paseo del Bosque SN, La Plata, 1900, Argentina

[b] Istituto Nazionale di Oceanografia e di Geofisica Sperimentale (OGS), Borgo Grotta Gigante 42c, 34010 Sgonico, Trieste, Italy

[c] CONICET, Instituto del Gas y del Petróleo, Facultad de Ingeniería, Universidad de Buenos Aires, Av. Las Heras 2214 Piso 3 C1127AAR Buenos Aires, Argentina

[d] Universidad Nacional de La Plata, La Plata, Argentina

[e] Department of Mathematics, Purdue University, 150 N. University Street, West Lafayette, IN, 47907-2067, USA

HIGHLIGHTS

- We model anisotropic behavior in porous media.
- We describe porous formations using poroelasticity theory and Backus averaging.
- We combine a domain decomposition technique with finite element method.
- We compare simulations of isotropic–elastic and anisotropic–anelastic seismograms.

ARTICLE INFO

Article history:
Received 31 May 2013
Received in revised form 11 December 2013
Accepted 1 January 2014
Available online 20 January 2014

Keywords:
Poroelasticity
Anisotropy
Viscoelasticity
Seismic waves
Finite elements method

ABSTRACT

In many cases, geological formations are composed of layers of dissimilar properties whose thicknesses are small compared to the wavelength of the seismic signal, as for instance, a sandstone formation that has intra-reservoir thin mudstone layers. A proper model is represented by an anisotropic (transversely isotropic) and viscoelastic stress–strain relation. In this work, we consider a sandstone reservoir, such as the Utsira formation, saturated with CO_2 and use White's mesoscopic model to describe the energy loss of the seismic waves. The mudstone layers are assumed to be isotropic, poroelastic and lossless. Then, Backus averaging provides the complex and frequency-dependent stiffnesses of the transversely isotropic (TI) long-wavelength equivalent medium. We obtain the associated wave velocities and quality factors as a function of frequency and propagation direction, while the synthetic seismograms are computed with a finite-element (FE) method in the space-frequency domain. In this way, the frequency-dependent properties of the medium are modeled exactly, without the need of approximations with viscoelastic mechanical models. Numerical simulations of synthetic seismograms show results in agreement with the predictions of the theories and significant differences due to attenuation and anisotropic effects compared to the ideal isotropic and lossless rheology.

1. Introduction

There is evidence that the concentration of CO_2 is one of the principal causes of the global warming and concurred to increase the atmospheric temperature by 0.3–0.6 °C during the last 150 years [1]. To solve this problem, geological

* Corresponding author. Tel.: +54 2214236593.
E-mail address: gauze@fcaglp.unlp.edu.ar (P.M. Gauzellino).

0165-2125/$ – see front matter © 2014 Elsevier B.V. All rights reserved.
http://dx.doi.org/10.1016/j.wavemoti.2014.01.001

sequestration is an immediate option. The possibilities are injection into hydrocarbon reservoirs, methane-bearing coal beds and saline aquifers. An example of the latter is the Sleipner field in the North Sea [2,3], where CO_2 is stored in the Utsira formation, a highly permeable porous sandstone 800 m below the sea bottom. The formation contains mudstone layers in the order of 0.5 m thick, which act as permeability barriers to the upward migration of the CO_2.

Since the layer thicknesses of such mudstone layers are much below the limit of seismic resolution, the long-wavelength approximation can be used, by which fine layering is equivalent to a homogeneous TI medium [4]. Carcione [5] generalized Backus averaging to the anelastic case by considering thin viscoelastic and isotropic layers, obtaining the first model for Q-anisotropy. Other alternative models of Q-anisotropy can be found in Carcione [6] (see also [7]). Backus's approach used by Carcione [5] is applied here, but the sandstone properties are obtained by using White's poroelastic model, which considers partial gas saturation [8] and yields a complex and frequency-dependent bulk modulus. It assumes that the medium has patches of gas in a brine saturated background and allows us to describe wave velocity and attenuation as a function of frequency, patch size, permeability and fluid viscosity. The associated relaxation mechanism has a peak at the seismic frequency range. On the other hand, the properties of the mudstone are described by a stress–strain relation based on the Gassmann equation [9,6]. Backus averaging gives the five complex stiffnesses of the TI medium. We obtain the quality factors and velocities as a function of frequency and propagation angle from these stiffnesses and the composite density. The theory for anisotropic and anelastic media is illustrated in [6].

Synthetic seismograms are computed by a domain decomposition method combined with a frequency domain FE method. This numerical procedure has already been applied to wave propagation in 2D and 3D media and to different rheological equations [10–13].

2. Properties of the equivalent TI medium

The sandstone complex and frequency-dependent Lamé constants are determined from a mesoscopic rock-physics theory [8], which provides realistic values as a function of porosity, gas saturation, clay content, fluid viscosity, permeability and patch size, r_1 (Appendix A). White assumed spherical gas pockets much larger than the grains but much smaller than the wavelength. He developed the theory for a gas-filled sphere of porous medium of radius r_0 located inside a water-filled cube of porous medium. For simplicity in the calculations, White [8] considered an outer sphere of radius r_1 ($r_1 > r_0$), instead of a cube, where $S_g = r_0^3/r_1^3$. More details can be found in White [8,9,14,6].

The mudstone layers are fully saturated with water and their properties are frequency independent. The acoustic properties are given by the Gassmann model [8,6], and the Lamé constants are

$$\lambda = \frac{K_s - K_m + \phi K_m \left(K_s/K_f - 1\right)}{1 - \phi - K_m/K_s + \phi K_s/K_f} - \frac{2}{3}\mu_m \quad \text{and} \quad \mu = \mu_m \tag{1}$$

where ϕ is the porosity, K_s and K_f are the bulk moduli of the grains and water, and K_m and μ_m are the dry-rock bulk and shear moduli, respectively. The P-wave modulus is

$$E = \lambda + 2\mu. \tag{2}$$

The density of the sandstone and mudstone is the arithmetic average of the density of the single constituents. Let ρ_s and ρ_f denote the mass densities of the solid grains and fluid, respectively. Then,

$$\rho = (1 - \phi)\rho_s + \phi\rho_f \tag{3}$$

denotes the bulk density of the single layers.

Fine layering on a scale much finer than the dominant wavelength of the signal yields effective anisotropy, whose elasticity constants are given by Backus averaging [4]. Carcione [5] uses this approach and the correspondence principle to study the anisotropic characteristics of attenuation in viscoelastic finely layered media (e.g., [6]). According to Carcione [5], the equivalent viscoelastic transversely isotropic medium is defined by the following complex stiffnesses and average density:

$$\begin{aligned}
p_{11} &= \langle E - \lambda^2 E^{-1}\rangle + \langle E^{-1}\rangle^{-1}\langle E^{-1}\lambda\rangle^2 \\
p_{33} &= \langle E^{-1}\rangle^{-1} \\
p_{13} &= \langle E^{-1}\rangle^{-1}\langle E^{-1}\lambda\rangle \\
p_{55} &= \langle \mu^{-1}\rangle^{-1} \\
p_{66} &= \langle \mu\rangle, \\
\bar{\rho} &= \langle \rho\rangle,
\end{aligned} \tag{4}$$

where $\langle\cdot\rangle$ denotes the thickness weighted average. The phase (energy) velocities and quality factors of the effective anisotropic and anelastic medium, which depend on frequency and propagation direction, are given in Appendix B. Let us define the wave properties associated with the symmetry axis perpendicular to the layering plane ($\theta = 0$) and with the direction along the layering plane ($\theta = \pi/2$). Components 33 and 11 correspond to the P wave, 55 to the SV wave and 55

and 66 to the SH wave for 0 and $\pi/2$, respectively (see Appendix B and [6]). Phase and energy velocities coincide along these directions. We have the following wave velocities and quality factors:

$$v_{II} = \left[\mathrm{Re}\left(\sqrt{\frac{\bar{\rho}}{p_{II}}}\right)\right]^{-1}, \quad I = 1, 3, 5, 6$$
$$Q_{II} = \frac{\mathrm{Re}(p_{II})}{\mathrm{Im}(p_{II})}. \tag{5}$$

3. The seismic modeling method

The algorithm used to simulate the wavefields is the FE method in the space-frequency domain, where the frequency-dependent anelastic effects can be described exactly without approximations [3,6]. Let us consider a 2D volume of an anisotropic and viscoelastic medium, $\Omega = [0, 1]^2$, with boundary $\Gamma = \partial\Omega$. Let $u(x, \omega)$ denote the displacement vector at the angular frequency ω. We consider the (x, z)-plane and the stress–strain relation describing a medium whose symmetry axis makes an angle ψ with the z-axis. This is obtained by a clockwise rotation of the vertical symmetry axis through an angle ψ about the y-axis, as indicated in Appendix C. Then, it can be shown that we have to consider the following stiffness matrix

$$\begin{pmatrix} p_{11} & p_{12} & p_{13} & 0 & p_{15} & 0 \\ p_{12} & p_{22} & p_{23} & 0 & p_{25} & 0 \\ p_{13} & p_{23} & p_{33} & 0 & p_{35} & 0 \\ 0 & 0 & 0 & p_{44} & 0 & 0 \\ p_{15} & p_{25} & p_{35} & 0 & p_{55} & 0 \\ 0 & 0 & 0 & 0 & 0 & p_{66} \end{pmatrix} \tag{6}$$

(see [6]).

The equation governing the motion is

$$-\rho(x)\omega^2 u(x, \omega) - \nabla \cdot \sigma[u(x, \omega)] = f(x, \omega), \quad x \in \Omega, \tag{7}$$

with absorbing boundary conditions

$$-\sigma[u(x, \omega)] \cdot \nu = \mathrm{i}\omega\sqrt{\rho}D^{1/2}u(x, \omega), \quad x \in \Gamma, \tag{8}$$

where

$$D = \frac{1}{2}\begin{pmatrix} 2p_{11}\nu_1^2 + p_{55}\nu_3^2 & 3(p_{15}\nu_1^2 + p_{35}\nu_3^2) \\ 3(p_{15}\nu_1^2 + p_{35}\nu_3^2) & p_{55}\nu_1^2 + 2p_{33}\nu_3^2 \end{pmatrix}. \tag{9}$$

In Eq. (7), σ and f represent the stress tensor and the external-source vector, respectively. The boundary Γ is transparent for normally incident waves and ν denotes the unit outward vector normal on Γ. The derivation can be found in [15] and Lovera and Santos [16].

We proceed to formulate the variational form of (7)–(8): find $u(x, \omega) \in [H^1(\Omega)]^2$ such that

$$-(\rho\omega^2 u, \varphi) + (\sigma(u), \varepsilon(\varphi)) + \mathrm{i}\omega\left\langle\sqrt{\rho}D^{1/2}u, \varphi\right\rangle_\Gamma = (f, \varphi), \quad \varphi \in [H^1(\Omega)]^2, \tag{10}$$

where ε is the strain tensor. Here $(f, g) = \int_\Omega fg^* dx$ and $\langle f, g^*\rangle = \int_\Gamma fg^* d\Gamma$ indicate the complex $[L^2(\Omega)]^2$ and $[L^2(\Gamma)]^2$ inner products, where "$*$" denotes the complex conjugate. $H^1(\Omega)$ denotes the usual Sobolev space of function in $L^2(\Omega)$ with first derivatives in $L^2(\Omega)$. The arguments given in Ha et al. [17] and Douglas et al. [10] can be used to show that the existence and uniqueness holds for the solution of (10).

Numerical dispersion is an important aspect to be taken into account when using wave propagation algorithms. It is shown in Zyserman et al. [18] that using the nonconforming FE space $\mathsf{N}\,\mathsf{C}^h$ described in [19] allows to use about half the number of points per wavelength to achieve a desired tolerance in numerical dispersion as compared with standard conforming bilinear elements. Thus, we will employ the FE space $\mathsf{N}\ C^h$ described below to compute an approximate solution of (10).

Let τ^h be a quasi-regular partition of $\bar{\Omega}$ such that $\bar{\Omega} = \cup_{j=1}^{J}\Omega_j$ with Ω_j being rectangles of diameter bounded by h. Set $\Gamma_j = \partial\Omega \cap \partial\Omega_j$ and $\Gamma_{jk} = \Gamma_{kj} = \partial\Omega_j \cap \partial\Omega_k$; we denote by ξ_j and ξ_{jk} the centroids of Γ_j and Γ_{jk}, respectively. Consider the reference rectangular element

$$R = [-1, 1]^2, \quad S(R) = \mathrm{Span}\left\{1, x, z, \left(x^2 - \frac{5}{3}x^4\right) - \left(z^2 - \frac{5}{3}z^4\right)\right\}.$$

The degrees of freedom associated with S are the values at the mid points of the faces of R. For example, if $a_1 = (-1, 0)$, $a_2 = (0, -1)$, $a_3 = (1, 0)$ and $a_4 = (0, 1)$, the basis function $\psi_1(x, z) = \frac{1}{4} - \frac{1}{2}x - \frac{3}{8}\left[(x^2 - \frac{5}{3}x^4) - (z^2 - \frac{5}{3}z^4)\right]$ is such that $\psi_1(a_1) = 1$ and $\psi_1(a_j) = 0, j = 2, 3, 4$. Then,

$$\mathsf{N}\,\mathsf{C}^h = \{\varphi \in [L^2(\Omega)]^2 : \varphi_j \in [S(\Omega_j)]^2,\ \varphi_j(\xi_{jk}) = \varphi_k(\xi_{jk})\ \forall j, k\},$$

where φ_j denotes the restriction of φ as seen from Ω_j.

Now the global nonconforming approximation u^h to the solution u of (10) can be stated as follows: find $u^h \in \mathsf{N}\,\mathsf{C}^h$ such that

$$-(\rho\omega^2 u^h, \varphi) + \sum_j (\sigma(u^h), \varepsilon(\varphi))_{\Omega_j} + \mathrm{i}\omega\left\langle\sqrt{\rho}D^{1/2}u^h, \varphi\right\rangle_{\Gamma} = (f, \varphi), \quad \varphi \in \mathsf{N}\,\mathsf{C}^h. \tag{11}$$

It can be shown (see [17] for the isotropic case) that for h sufficiently small the error associated with the global procedure (11) is of order h^2 in the L^2-norm and of order h in the broken H^1-energy norm.

Note that (11) is a noncoercive elliptic Helmholtz-type problem, so that the usual iterative procedures like preconditioned conjugate gradient iterative algorithms cannot be used. Consequently, to solve the algebraic problem associated with the global nonconforming procedure (11), we will employ the iterative domain decomposition procedure described below.

Remark. In addition to the low numerical dispersion properties of the space $\mathsf{N}\,\mathsf{C}^h$, one of the main advantages of using nonconforming elements to solve wave propagation phenomena in parallel architectures is that the amount of information exchanged in a domain decomposition iterative procedure is reduced by half as compared to the case when conforming elements are employed.

Consider the decomposed problem over Ω_j satisfying Eq. (7) in Ω_j, the boundary condition

$$-\sigma[u_j(x, \omega)] \cdot \nu = \mathrm{i}\omega\sqrt{\rho}D^{1/2}u_j(x, \omega), \quad x \in \Gamma_j,$$

and the interface consistency conditions

$$\sigma_{jk}\nu_{jk} + \mathrm{i}\beta_{jk}u_j = -\sigma_{kj}\nu_{kj} + \mathrm{i}\beta_{jk}u_k, \quad x \in \Gamma_{jk} \subset \partial\Omega_j,$$
$$\sigma_{kj}\nu_{kj} + \mathrm{i}\beta_{jk}u_k = -\sigma_{jk}\nu_{jk} + \mathrm{i}\beta_{jk}u_j, \quad x \in \Gamma_{kj} \subset \partial\Omega_k,$$

where β_{jk} are the components of a positive definite matrix function defined on the interior boundaries Γ_{jk}. The iteration matrix β_{jk}, defined on the interior interfaces Γ_{jk} can be taken to be of the same form as the matrix D in (9) using averaged properties of the coefficients defining D on the adjacent elements Ω_j and Ω_k.

Since the objective of the domain decomposition technique is to localize the calculations, we define the iterative procedure at the differential level in the following manner: find $u_j^n \in [H^1(\Omega_j)]^2$ such that

$$(-\rho\omega^2 u_j^n, \varphi)_j + \sum_j \sum_{pq} (\sigma_{pq}(u_j^n), \varepsilon_{pq}(\varphi))_j + \left\langle\mathrm{i}\omega\sqrt{\rho}D^{1/2}u_j^n, \varphi\right\rangle_{\Gamma_j}$$
$$+ \sum_k \langle[\sigma(u_k^{n-1})\nu_{jk} + \mathrm{i}\beta_{jk}(u_j^n - u_k^{n-1})], \varphi\rangle_{\Gamma_{jk}} = (f, \varphi)_j, \quad \varphi \in [H^1(\Omega_{jk})]^2. \tag{12}$$

To define a discrete iterative procedure we introduce a set Λ^h of Lagrange multipliers λ_{jk}^h associated with the stress values $-\sigma(u_j)\nu_{jk}(\xi_{jk})$:

$$\Lambda^h = \{\lambda^h : \lambda^h|_{\Gamma_{jk}} = \lambda_{jk}^h \in [P_0(\Gamma_{jk})]^2 = [\Lambda_{jk}^h]^2\};$$

here, $P_0(\Gamma_{jk})$ are constant functions on Γ_{jk}.

Motivated by (12), we define the following discrete domain decomposition (hybridized) iterative algorithm:

(1) Choose an initial guess $\left(u_j^{h,0}, \lambda_{jk}^{h,0}, \lambda_{kj}^{h,0}\right) \in NC_j^h \times [\Lambda_{jk}^h]^2 \times [\Lambda_{kj}^h]^2$.

(2) For all $\{jk\}$, compute $\left(u_j^{h,n}, \lambda_{jk}^{h,n} \in NC_j^h \times \Lambda_{jk}^h\right)$ as the solution of the equations

$$-(\rho\omega^2 u_j^{h,n}, \varphi)_{jk} + \sum_{pq} (\sigma_{pq}(u_j^{h,n}), \varepsilon_{pq}(\varphi))_{jk} + \mathrm{i}\omega\left\langle\!\!\left\langle\sqrt{\rho}D^{1/2}u_j^{h,n}, \varphi\right\rangle\!\!\right\rangle_{\Gamma_j}$$
$$+ \sum_k \left\langle\!\!\left\langle\lambda_{jk}^{h,n}, \varphi\right\rangle\!\!\right\rangle_{\Gamma_{jk}} = (f, \varphi)_j, \quad \varphi \in NC_j^h \tag{13}$$

and

$$\lambda_{jk}^{h,n} = -\lambda_{kj}^{h,n-1} + \mathrm{i}\beta_{jk}[u_j^{h,n}(\xi_{jk}) - u_k^{h,n-1}(\xi_{jk})], \quad \text{on } \Gamma_{jk}. \tag{14}$$

Table 1
Properties of the Utsira formation.

	Sandstone	Mudstone
Grain bulk modulus, K_s (GPa)	40	20
Density, ρ_s (kg/m^3)	2600	2600
Frame bulk modulus, K_m (GPa)	1.37	7
Shear modulus, μ_m (GPa)	0.82	6
Porosity, ϕ	0.36	0.2
Permeability, κ (D)	1.6	–
Brine density, ρ_w (kg/m^3)	1030	1030
Viscosity, η_w (Pa s)	0.0012	–
Bulk modulus, K_w (GPa)	2.6	2.6
CO_2 density, ρ_g (kg/m^3)	505	–
Viscosity, η_g (Pa s)	0.00015	–
Bulk modulus, K_g (MPa)	25	–

In (13) $\langle\langle\cdot,\cdot\rangle\rangle_{\Gamma_{jk}}$ denote the approximation to the (complex) inner product $\langle\cdot,\cdot\rangle_{\Gamma_{jk}}$ in $L^2(\Gamma_{jk})$ computed using the mid-point quadrature rule. More precisely,

$$\langle\langle u, v\rangle\rangle_{\Gamma_{jk}} = (uv^*)(\xi_{jk})|\Gamma_{jk}|, \tag{15}$$

where $|\Gamma_{jk}|$ is the surface measure of Γ_{jk}. A similar definition holds for $\langle\langle\cdot,\cdot\rangle\rangle_{\Gamma_j}$, changing in (15) ξ_{jk} and Γ_{jk} by ξ_j and Γ_j, respectively.

The argument given in [17] for isotropic viscoelastic solids can be applied here with minor modifications to show that

$$[u^{h,n} - u^h] \to 0 \quad \text{in } [L^2(\Omega)]^2 \text{ if } \to \infty,$$

so that in the limit the global nonconforming Galerkin approximation u^h of (11) is obtained.

3.1. Computational implementation

The size of the subdomains of the decomposition, and therefore the number of elements considered within each of them can be varied. If the smallest subdomain coincides with the individual elements of the finite element partition, the number of degrees of freedom and the order of the linear system originated by Eq. (13) is eight.

But, in according to the analyses carried out by Gauzellino et al. [20], in this implementation we consider each subdomain as a row or "stripe" of Nx elements, Nx being the number of elements fitting in the x-coordinate direction of Ω. In this case the order of the linear system associated with each "stripe" is $6Nx + 2$ and a standard LU method is used to solve it, i.e., essentially we solve a collection of 1D problems. In order to improve the convergence rate, an under relaxed "red–black" scheme is employed. We divide the "stripes" into two sets, called "red" and "black" ones, where each red subdomain has only as neighbors black subdomains. The linear system obtained using Eq. (13) is solved first for the red stripes and the black stripe neighbors contribute to form its corresponding right hand side. Then, red Lagrange multipliers are updated using Eq. (14) and all the variables, $u_j^{h,n}$ and $\lambda_{jk}^{h,n}$ are under relaxed by the expressions

$$u_j^n = \gamma u_j^n + (1-\gamma)u_j^{n-1}, \qquad \lambda_{jk}^n = \gamma\lambda_{jk}^n + (1-\gamma)\lambda_{jk}^{n-1}, \tag{16}$$

respectively. The relaxation factor, γ, has an optimal value that is determined through numerical experiments. The same technique is employed to solve the black stripes; once the red and black stripes are fulfilled convergence is checked. The convergence of this domain decomposition iterative procedure was demonstrated in [17] for the isotropic case; the arguments can be extended here without changes. Also, the performance of the algorithm was studied in [20].

4. Results

We consider the properties of the Utsira formation shown in Table 1, alternating layers of mudstone and sandstone of equal thickness, $r_1 = 20$ cm and $f_0 = 30$ Hz. The energy velocity (a) and dissipation factor (b) of the different wave modes as a function of frequency are shown in Figs. 1 and 2.

On the other hand, Figs. 3 and 4 display the polar representation of the energy velocity (a) and quality factor (b) corresponding to a frequency of 30 Hz and 50% and 10% CO_2 saturation, respectively. The P wave shows high attenuation at $\theta = 0$ compared to $\theta = \pi/2$, while maximum attenuation occurs at low gas saturations.

Since geological formations have a structural dip angle due to tectonic stresses, we need to obtain the values of the stiffness components at different orientations of the symmetry axis of the TI medium. This process is shown in Appendix C.

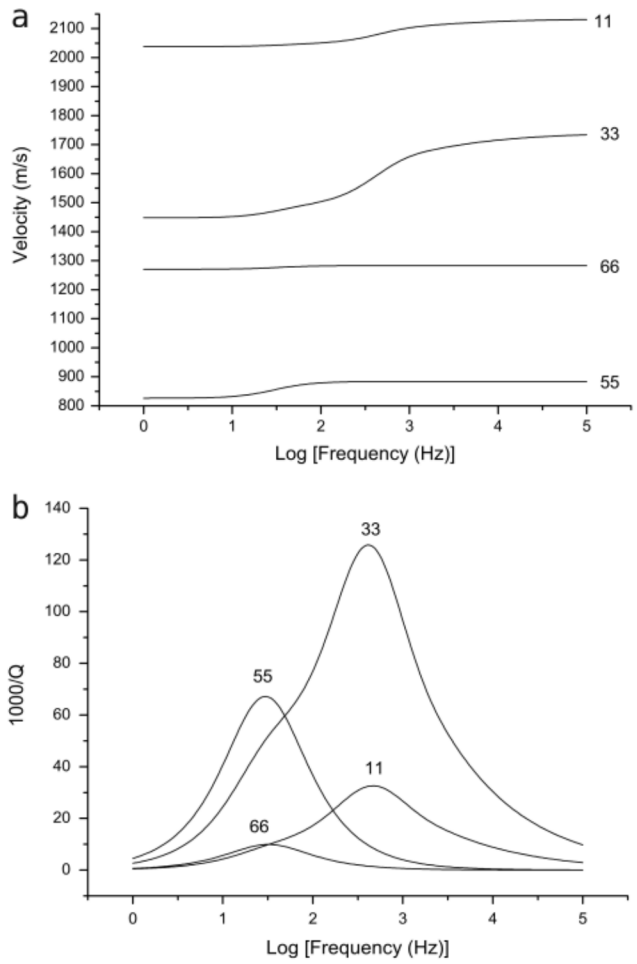

Fig. 1. Energy velocity (a) and dissipation factor (b) versus frequency, perpendicular and parallel to the layering plane. The CO_2 saturation is 0.5.

Then, the modeling can describe a different layer orientation at each grid cell. Let us consider the case of 50% saturation and a frequency of 30 Hz. The stiffness tensor is

$$\mathbf{P} = \begin{pmatrix} (8.81, 0.084) & (2.69, 0.025) & (1.26, 0.038) & 0 & 0 & 0 \\ (2.69, 0.025) & (8.81, 0.084) & (1.26, 0.038) & 0 & 0 & 0 \\ (1.26, 0.038) & (1.26, 0.038) & (4.56, 0.23) & 0 & 0 & 0 \\ 0 & 0 & 0 & (1.54, 0.10) & 0 & 0 \\ 0 & 0 & 0 & 0 & (1.54, 0.10) & 0 \\ 0 & 0 & 0 & 0 & 0 & (3.44, 0.0034) \end{pmatrix} \tag{17}$$

(in GPa). For instance, a rotation of the symmetry axis by 20° gives

$$\mathbf{P}' = \begin{pmatrix} (7.83, 0.12) & (2.52, 0.027) & (1.74, 0.020) & 0 & (-1.26, 0.045) & 0 \\ (2.52, 0.027) & (8.81, 0.084) & (1.43, 0.037) & 0 & (-0.46, 0.0041) & 0 \\ (1.74, 0.020) & (1.43, 0.037) & (4.56, 0.23) & 0 & (-0.11, 0.0022) & 0 \\ 0 & 0 & 0 & (1.76, 0.10) & 0 & (-0.61, 0.022) \\ (-1.26, 0045) & (-0.46, 0.0041) & (-0.11, 0.0022) & 0 & (2.02, 0.085) & 0 \\ 0 & 0 & 0 & (-0.61, 0.022) & 0 & (3.21, 0.042) \end{pmatrix} \tag{18}$$

(in GPa).

To compute the transient responses, we use as a source a Ricker time history of the form:

$$f(t) = \left(a - \frac{1}{2}\right)\exp(-a), \quad a = \left[\frac{\pi(t - t_s)}{t_0}\right]^2, \tag{19}$$

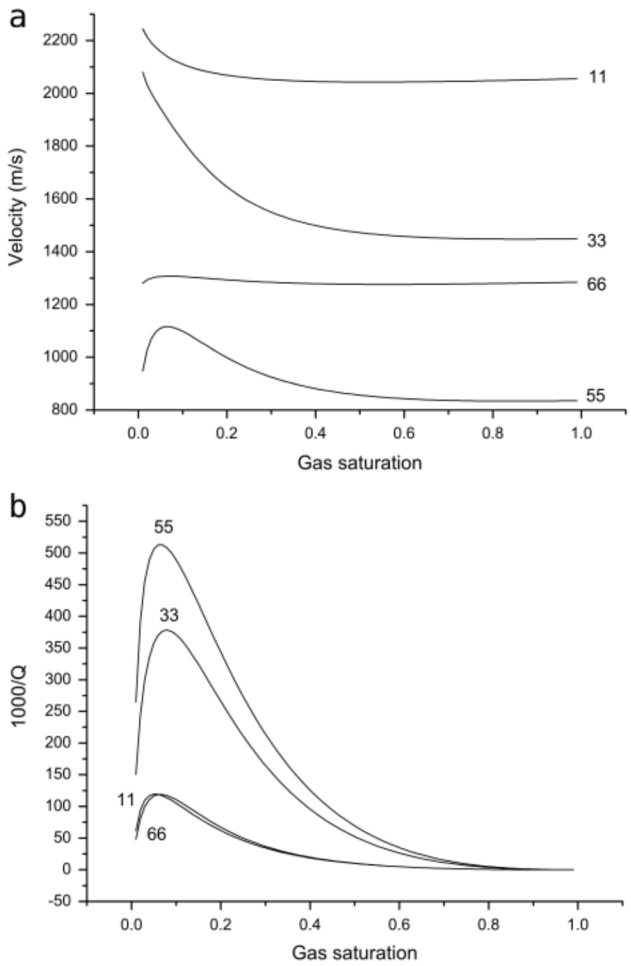

Fig. 2. Energy velocity (a) and dissipation factor (b) versus CO_2 saturation perpendicular and parallel to the layering plane. The frequency is 30 Hz.

where t_0 is the period of the wave (the distance between the side peaks is $\sqrt{6}t_0/\pi$) and we take $t_s = 1.4t_0$. Its frequency spectrum is

$$F(\omega) = \left(\frac{t_0}{\sqrt{\pi}}\right)\bar{a}\exp(-\bar{a} - \mathrm{i}\omega t_s), \quad \bar{a} = \left(\frac{\omega}{\omega_0}\right)^2, \qquad \omega_p = \frac{2\pi}{t_0}. \tag{20}$$

The peak frequency is $f_0 = 1/t_0$.

First, we consider a homogeneous viscoelastic medium and compute snapshots of the wavefield. The simulations consider a square computational domain of 1 km side and a partition of the domain into square cells.

In the first example, the square cells have side length 2 m and the source is a directional force, located at the center of the mesh, with components $f_x = \sin\varphi$ and $f_z = \cos\varphi$, where φ is the angle with respect to the z-axis. The source central frequency is $f_0 = 30$ Hz. The solution was computed for 160 frequencies in the range 0–80 Hz, with a frequency sampling of 0.5 Hz. The time domain solution was obtained using a discrete inverse Fourier transform.

Fig. 5 shows snapshots of the horizontal and vertical displacements at 250 ms, where the qP and qSV waves can be observed (outer and inner fronts, respectively). The medium has been rotated by $\psi = 20^\circ$ and the source has $\varphi = 20^\circ$. The saturation of CO_2 is 10% ((a) and (b)) and 50% ((c) and (d)). It can be seen that the features of the snapshots agree with the predictions of the plane-wave analysis represented by Figs. 3 and 4. In fact, a lower frequency content can be appreciated in Fig. 5(a)–(b), where the CO_2 saturation is 10% and the attenuation is high, compared to Fig. 5(c)–(d), where the saturation is 50% and the attenuation is low.

In the second example, we present a simplified model composed of an anisotropic layer between two half-spaces. The upper half space is an isotropic and elastic medium with P- and S-wave velocities equal to 1890 m/s and 592 m/s, respectively, and a density of 2100 kg/m^3. The layer, with a thickness of 300 m, is the anisotropic and anelastic medium whose single components are given in Table 1. The medium is rotated by 20°, i.e., the angle between the symmetry axis and the vertical direction. The lower half-space has P- and S-wave velocities of 2320 m/s and 730 m/s, respectively, and a

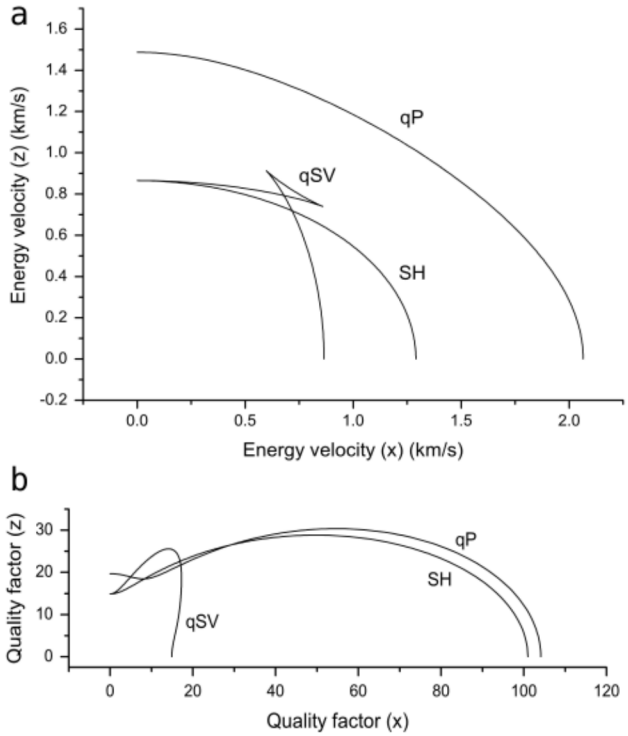

Fig. 3. Polar representation of the energy velocity (a) and quality factor (b) corresponding to a frequency of 30 Hz and 50% CO_2 saturation. The quality factor is shown as a function of the phase angle.

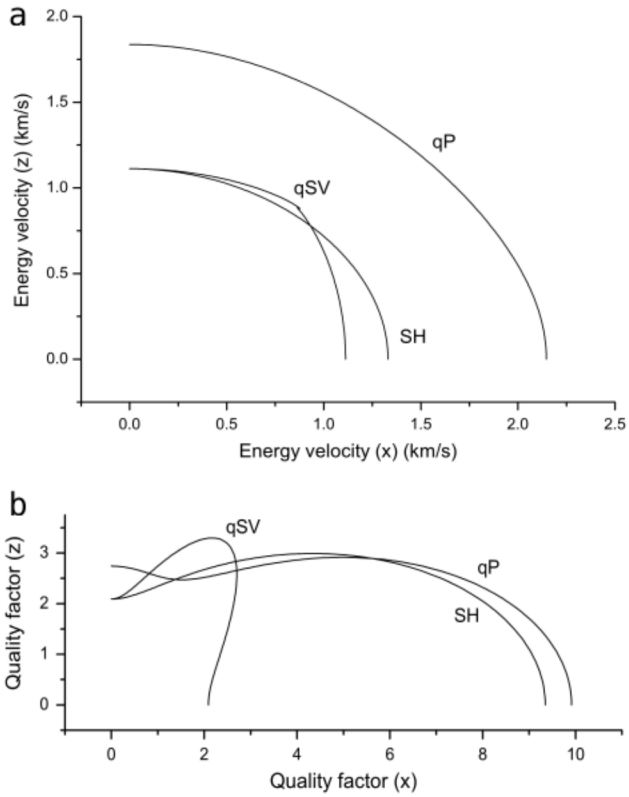

Fig. 4. Polar representation of the energy velocity (a) and quality factor (b) corresponding to a frequency of 30 Hz and 10% CO_2 saturation. The quality factor is shown as a function of the phase angle.

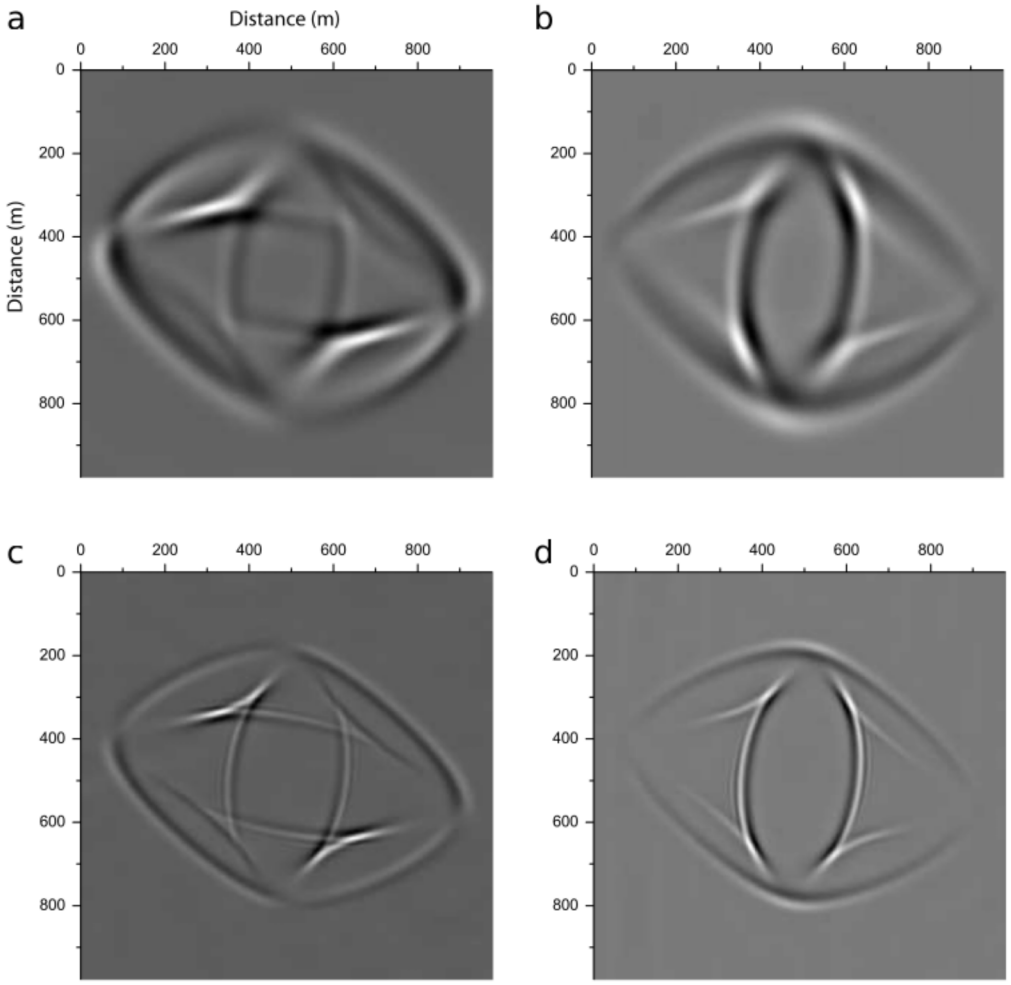

Fig. 5. Snapshots of the horizontal ((a) and (c)) and vertical ((b) and (d)) displacements corresponding to a central source frequency of 30 Hz. The medium is rotated by $\psi = 20^\circ$ and the source is a directional force making an angle of 20° with respect to the z-axis, located at the center of the mesh. The saturation of CO_2 is 10% ((a) and (b)) and 50% ((c) and (d)).

density of 2300 kg/m^3. The square cells have side length 3.7 m and the source is a dilatational perturbation indicated with an asterisk in the snapshots shown in Fig. 6, where the interfaces are indicated. Its central frequency is 30 Hz and it is located 150 m below the first interface. The vertical line, labeled A, represents a well at 400 m from the source location. The first receiver is located at 500 m above the first interface and the distance between adjacent receivers is 21.3 m. The solution was computed for 900 frequencies in the range 0–80 Hz, with a frequency sampling of 0.088 Hz. Absorbing boundaries are implemented at the four sides of the mesh. The snapshots in Fig. 6 represent the vertical component of the displacement vector at 200 ms ((a) and (c)) and 500 ms ((b) and (d)) propagation time with an isotropic–elastic (lossless) stress–strain relation ((a) and (b)) and the more realistic anisotropic–viscoelastic relation developed in this work ((c) and (d)).

The seismograms recorded at the well are displayed in Figs. 7 (isotropic–elastic media) and 8 (anisotropic–viscoelastic media). The ideal seismograms correspond to an elastic and isotropic stress–strain relation, taking the elastic case at the high frequency limit. The labels indicate:

P: Direct P waves through the layer.
S: Direct S waves through the layer.
P_R: Reflected P wave.
S_R: Reflected S wave.
P_T: Transmitted P.
S_T: Transmitted S.
PS_T: Transmitted P to S wave conversion.

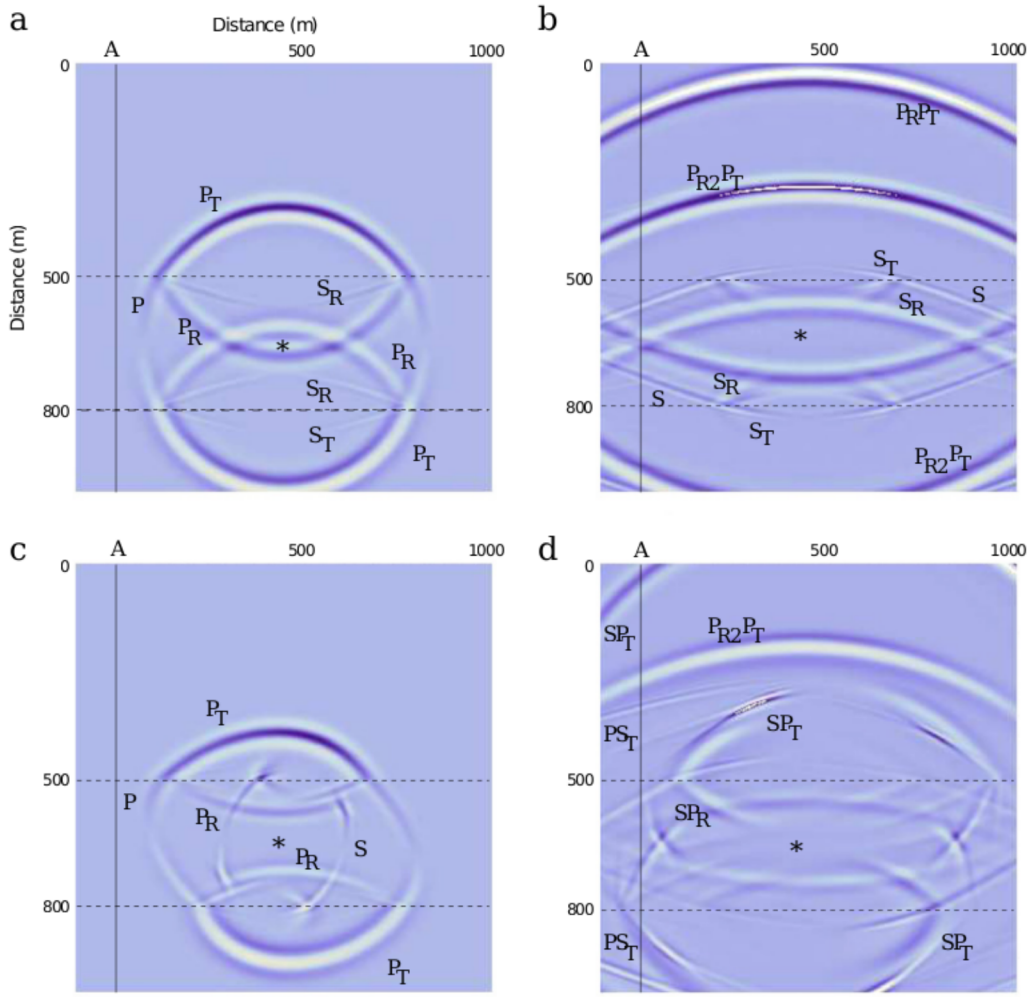

Fig. 6. Snapshots of the vertical displacement at 200 ms ((a) and (c)) and 500 ms ((b) and (d)) propagation time, corresponding to the ideal case ((a) and (b)) and real case ((c) and (d)). Most of the labels are explained in the main text; S_R and S_T in (a) indicate a mode conversion.

SP_T: Transmitted S to P wave conversion.
PS_R: Reflected P to S wave conversion.
P_RP_T: Reflected P wave through the layer to transmitted P wave.
$P_{R2}P_T$: Reflected P wave twice through the layer to transmitted P wave.

The reflected P waves in the second layer are better observed in the vertical displacement while converted waves are more evident in the horizontal displacement. In Fig. 8, it can be observed a significant loss of energy due to the attenuation. As can be seen, the differences are substantial, indicating that a real rheological equation is required to interpret data related to this specific problem.

5. Conclusions

The anisotropic and anelastic properties of the reservoir rocks, aquifers and other porous formations are described by using poroelasticity theory (White's mesoscopic model) and Backus averaging, in order to model the anisotropic behavior of finely-layered media at long wavelengths. A typical case is the Utsira formation in the North Sea area, consisting of a sequence of sandstone layers partially saturated with CO_2 and brine-saturated mudstone layers. Here, we have obtained the complex and frequency-dependent stiffnesses and density, which allow us to compute the wave velocities and quality factors as a function of frequency and propagation angle.

Moreover, we compare snapshots and synthetic seismograms for varying saturations and ideal and real rheological equations, i.e., isotropic–elastic and anisotropic–anelastic, respectively. The modeling methodology is based on a finite-

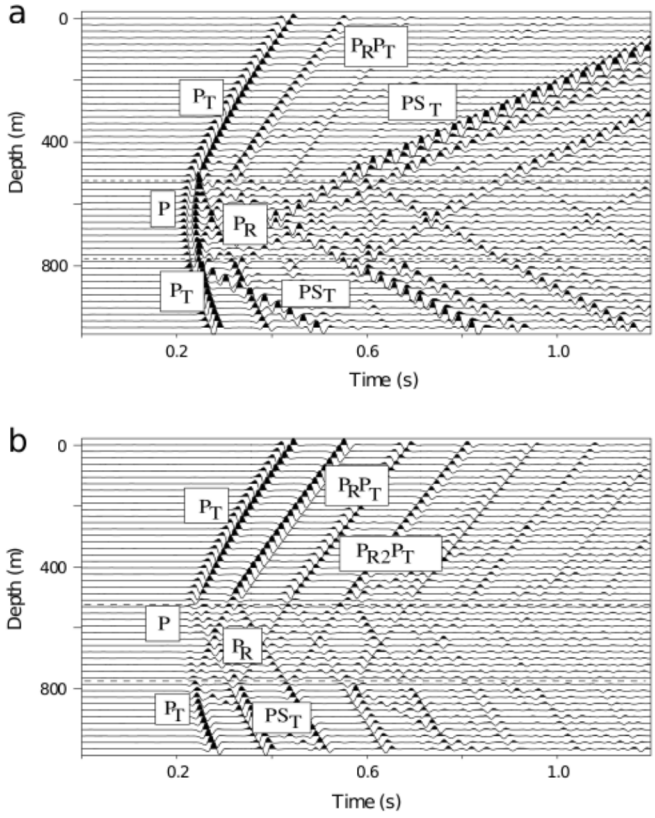

Fig. 7. Seismograms of the horizontal (a) and vertical (b) displacements, corresponding to the ideal (isotropic–elastic) case. The labels are explained in the main text.

element solution of the equations of motion in the space-frequency domain. Hence, the frequency dependence of the seismic properties is modeled exactly, without approximations used in the time domain (e.g., memory variables based on mechanical models).

The theory and numerical solver proposed in this work can be applied to more complex geological situations (lower symmetries, stochastic heterogeneities, fractures, etc.) and implemented in the processing and interpretation of real seismic data for characterization purposes.

Acknowledgments

This work has been partially funded by the CO2REMOVE and CO2CARE projects.

Appendix A. White's mesoscopic model including S-wave dissipation

White [8] assumed spherical patches much larger than the grains but much smaller than the wavelength. He developed the theory for a gas-filled sphere of porous medium of radius r_0 located inside a water-filled sphere (brine here) of porous medium of outer radius r_1 ($r_0 < r_1$). The saturation of gas is

$$S_g = \frac{r_0^3}{r_1^3}, \qquad S_b = 1 - S_g. \tag{A.1}$$

For simplicity, let us redefine the saturation and density of gas and brine by S_1 and S_2 and ρ_{f1} and ρ_{f2}, respectively.

Assuming that the dry-rock and grain moduli and permeability, κ, of the different regions are the same, the complex bulk modulus as a function of frequency is given by [9,14],

$$K = \frac{K_\infty}{1 - K_\infty W}, \tag{A.2}$$

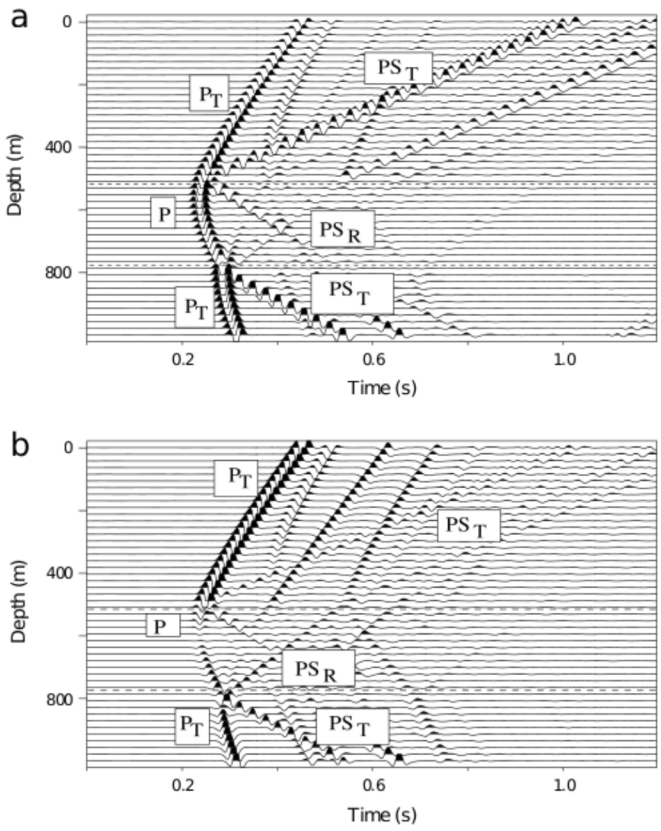

Fig. 8. Seismograms of the horizontal (a) and vertical (b) displacements, corresponding to the real (anisotropic–anelastic) case. The labels are explained in the main text.

where

$$
\begin{aligned}
W &= \frac{3ir_0\kappa(R_1-R_2)}{r_1^3\omega(\eta_1 Z_1-\eta_2 Z_2)}\left(\frac{K_{A1}}{K_1}-\frac{K_{A2}}{K_2}\right),\\
R_1 &= \frac{(K_1-K_m)(3K_2+4\mu_m)}{K_2(3K_1+4\mu_m)+4\mu_m(K_1-K_2)S_1},\\
R_2 &= \frac{(K_2-K_m)(3K_1+4\mu_m)}{K_2(3K_1+4\mu_m)+4\mu_m(K_1-K_2)S_1},\\
Z_1 &= \frac{1-\exp(-2\gamma_1 r_0)}{(\gamma_1 r_0-1)+(\gamma_1 r_0+1)\exp(-2\gamma_1 r_0)},\\
Z_2 &= \frac{(\gamma_2 r_1+1)+(\gamma_2 r_1-1)\exp[2\gamma_2(r_1-r_0)]}{(\gamma_2 r_1+1)(\gamma_2 r_0-1)-(\gamma_2 r_1-1)(\gamma_2 r_0+1)\exp[2\gamma_2(r_1-r_0)]},\\
\gamma_j &= \sqrt{i\omega\eta_j/(\kappa K_{Ej})},\\
K_{Ej} &= \left[1-\frac{\alpha K_{fj}(1-K_j/K_s)}{\phi K_j(1-K_{fj}/K_s)}\right]K_{Aj},\\
K_{Aj} &= \left[\frac{\phi}{K_{fj}}+\frac{1}{K_s}(\alpha-\phi)\right]^{-1}, \quad j=1,2,\\
\alpha &= 1-\frac{K_m}{K_s},
\end{aligned}
\tag{A.3}
$$

K_s is the bulk modulus of the grains (see below), K_{fj} are the bulk moduli of the fluids, η_j are the fluid viscosities, K_m and μ_m are the dry-rock bulk and shear moduli, respectively and

$$
K_\infty = \frac{K_2(3K_1+4\mu_m)+4\mu_m(K_1-K_2)S_1}{(3K_1+4\mu_m)-3(K_1-K_2)S_1} \tag{A.4}
$$

is the – high frequency – bulk modulus when there is no fluid flow between the patches. K_1 and K_2 are the – low frequency – Gassmann moduli, which are obtained as

$$K_j = \frac{K_s - K_m + \phi K_m \left(K_s/K_{fj} - 1\right)}{1 - \phi - K_m/K_s + \phi K_s/K_{fj}}, \quad j = 1, 2. \tag{A.5}$$

For values of the gas saturation higher than 52%, or values of the water saturation between 0% and 48%, the theory is not rigorously valid. Another limitation to consider is that the size of gas pockets should be much smaller than the wavelength.

Since White's theory does not predict any shear dissipation, we assume that the complex modulus μ is described by a Zener element having a peak frequency f_0 (the source central frequency) and a minimum quality factor given by

$$Q_0^{(2)} = \frac{\mu_m}{K_m} Q_0, \tag{A.6}$$

where Q_0 is the quality factor associated with K at f_0, i.e.,

$$Q_0 = Q(f_0) = \frac{\mathrm{Re}[K(f_0)]}{\mathrm{Im}[K(f_0)]}. \tag{A.7}$$

Relation (A.6) assumes that the stiffest medium has the highest quality factor.

Then, the Zener complex modulus is

$$M = \frac{1 + \mathrm{i}\omega\tau_\epsilon}{1 + \mathrm{i}\omega\tau_\sigma}, \tag{A.8}$$

where ω is the angular frequency and $\mathrm{i} = \sqrt{-1}$.

The relaxation times can be expressed as

$$\tau_\epsilon = \frac{\tau_0}{Q_0^{(2)}} \left(\sqrt{(Q_0^{(2)})^2 + 1} + 1 \right), \qquad \tau_\sigma = \tau_\epsilon - \frac{2\tau_0}{Q_0^{(2)}}, \tag{A.9}$$

where τ_0 is a relaxation time such that $1/\tau_0$ is the center frequency of the relaxation peak and Q_0 is the minimum quality factor. The frequency f_0 is taken in the seismic frequency range in this work, particularly, equal to the source dominant frequency.

The complex Lamé constants are given by

$$\begin{aligned} \lambda &= K - (2/3)\mu, \\ \mu &= \mu_m M, \end{aligned} \tag{A.10}$$

and

$$E = \lambda + 2\mu \tag{A.11}$$

is the P-wave modulus.

Appendix B. Wave velocities and quality factors

We consider homogeneous viscoelastic waves [6]. The complex velocities are the key quantity to obtain the wave velocities and the quality factor of the equivalent anisotropic medium. They are given by [6]

$$\begin{aligned} v_{\mathrm{qP}} &= (2\bar{\rho})^{-1/2} \sqrt{p_{11} l_1^2 + p_{33} l_3^2 + p_{55} + A} \\ v_{\mathrm{qSV}} &= (2\bar{\rho})^{-1/2} \sqrt{p_{11} l_1^2 + p_{33} l_3^2 + p_{55} - A} \\ v_{\mathrm{SH}} &= \bar{\rho}^{-1/2} \sqrt{p_{66} l_1^2 + p_{55} l_3^2} \\ A &= \sqrt{[(p_{11} - p_{55}) l_1^2 + (p_{55} - p_{33}) l_3^2]^2 + 4[(p_{13} + p_{55}) l_1 l_3]^2}, \end{aligned} \tag{B.1}$$

where $l_1 = \sin\theta$ and $l_3 = \cos\theta$ are the direction cosines, θ is the propagation angle between the wavenumber vector and the symmetry axis, and the three velocities correspond to the qP, qS and SH waves, respectively. The phase velocity is given by

$$v_p = \left[\mathrm{Re}\left(\frac{1}{v}\right) \right]^{-1}, \tag{B.2}$$

where v represents either v_{qP}, v_{qSV} or v_{SH}. The energy-velocity vector of the qP and qSV waves is given by

$$\frac{\mathbf{v}_e}{v_p} = (l_1 + l_3 \cot\psi)^{-1}\hat{\mathbf{e}}_1 + (l_1 \tan\psi + l_3)^{-1}\hat{\mathbf{e}}_3, \tag{B.3}$$

[6, Eq. 6.158], where

$$\tan\psi = \frac{\mathrm{Re}(\beta^* X + \xi^* W)}{\mathrm{Re}(\beta^* W + \xi^* Z)}, \tag{B.4}$$

defines the angle between the energy-velocity vector and the z-axis,

$$\begin{aligned} &\beta = \sqrt{A \pm B}, \\ &\xi = \pm \mathrm{pv}\sqrt{A \mp B}, \\ &B = p_{11} l_1^2 - p_{33} l_3^2 + p_{55}\cos 2\theta, \end{aligned} \tag{B.5}$$

where the upper and lower signs correspond to the qP and qS waves, respectively. Moreover,

$$\begin{aligned} &W = p_{55}(\xi s_1 + \beta s_3), \\ &X = \beta p_{11} s_1 + \xi p_{13} s_3, \\ &Z = \beta p_{13} s_1 + \xi p_{33} s_3 \end{aligned} \tag{B.6}$$

[6, Eqs. 6.121–6.123], where $s_1 = s l_1$ and $s_3 = s l_3$, with $s = 1/v$, are the slowness components and "pv" denotes the principal value, which has to be chosen according to established criteria.

On the other hand, the energy velocity of the SH wave is

$$\mathbf{v}_e = \frac{v_p}{\rho \mathrm{Re}(v)}\left[l_1 \mathrm{Re}\left(\frac{p_{66}}{v}\right)\hat{\mathbf{e}}_1 + l_3 \mathrm{Re}\left(\frac{p_{55}}{v}\right)\hat{\mathbf{e}}_3\right] \tag{B.7}$$

and

$$\tan\psi = \frac{\mathrm{Re}(p_{66}/v)}{\mathrm{Re}(p_{55}/v)}\tan\theta \tag{B.8}$$

[6, Eq. 4.115].

In general, we have the property

$$v_p = v_e \cos(\psi - \theta), \tag{B.9}$$

where $v_e = |\mathbf{v}_e|$. The quality factor is given by

$$Q = \frac{\mathrm{Re}(v^2)}{\mathrm{Im}(v^2)}. \tag{B.10}$$

The values of the qP quality factor along the layering plane and symmetry axis are

$$Q_P(\theta = \pi/2) = \frac{\mathrm{Re}(p_{11})}{\mathrm{Im}(p_{11})} \quad \text{and} \quad Q_P(\theta = 0) = \frac{\mathrm{Re}(p_{33})}{\mathrm{Im}(p_{33})}, \tag{B.11}$$

respectively, while those of the shear waves are

$$Q_{SV}(\theta = \pi/2) = Q_{SV}(\theta = 0) = Q_{SH}(\theta = 0) = \frac{\mathrm{Re}(p_{55})}{\mathrm{Im}(p_{55})}, \quad \text{and} \quad Q_{SH}(\theta = \pi/2) = \frac{\mathrm{Re}(p_{66})}{\mathrm{Im}(p_{66})}. \tag{B.12}$$

Appendix C. Rotation of the stiffness tensor

In geological media, the symmetry axis of the TI medium is usually not vertical due to local tectonic stresses. In this case, a rotation of the stiffness tensor is required. For a vertical symmetry axis along the z-axis, this is given by

$$\mathbf{P} = \begin{pmatrix} p_{11} & p_{12} & p_{13} & 0 & 0 & 0 \\ p_{12} & p_{11} & p_{13} & 0 & 0 & 0 \\ p_{13} & p_{13} & p_{33} & 0 & 0 & 0 \\ 0 & 0 & 0 & p_{55} & 0 & 0 \\ 0 & 0 & 0 & 0 & p_{55} & 0 \\ 0 & 0 & 0 & 0 & 0 & p_{66} \end{pmatrix}, \qquad 2p_{66} = p_{11} - p_{12}. \tag{C.1}$$

A clockwise rotation of the vertical symmetry axis through an angle ψ about the y-axis has the orthogonal transformation matrix

$$\mathbf{A} = \begin{pmatrix} \cos\psi & 0 & \sin\psi \\ 0 & 1 & 0 \\ -\sin\psi & 0 & \cos\psi \end{pmatrix}. \tag{C.2}$$

The corresponding Bond transformation matrix is [6],

$$\mathbf{M} = \begin{pmatrix} \cos^2\psi & 0 & \sin^2\psi & 0 & \sin(2\psi) & 0 \\ 0 & 1 & 0 & 0 & 0 & 0 \\ \sin^2\psi & 0 & \cos^2\psi & 0 & -\sin(2\psi) & 0 \\ 0 & 0 & 0 & \cos\psi & 0 & -\sin\psi \\ -\frac{1}{2}\sin(2\psi) & 0 & \frac{1}{2}\sin(2\psi) & 0 & \cos(2\psi) & 0 \\ 0 & 0 & 0 & \sin\psi & 0 & \cos\psi \end{pmatrix}. \tag{C.3}$$

Then, the stiffness matrix with the rotated symmetry axis is given by [6],

$$\mathbf{P}' = \mathbf{M} \cdot \mathbf{P} \cdot \mathbf{M}^{\top}. \tag{C.4}$$

References

[1] T.S. Ledley, E.T. Sundquist, S.E. Schwartz, D.K. Hall, J.D. Fellows, T.L. Killeen, Climate change and greenhouse gases, EOS Trans. Am. Geophys. Union 80 (1999) 453–458.
[2] R. Arts, O. Eiken, R.A. Chadwick, P. Zweigel, L. van Der Meer, G.A. Kirby, Seismic monitoring at the Sleipner underground CO_2 storage site (North Sea), in: S. Baines, R.J. Worden (Eds.), Geological Storage for CO_2 Emissions Reduction: Special Publication of the Geological Society of London, vol. 233, 2004, pp. 181–191.
[3] J.M. Carcione, S. Picotti, D. Gei, G. Rossi, Physics and seismic modeling for monitoring CO_2 storage, Pure Appl. Geophys. 163 (2006) 175–207.
[4] G.E. Backus, Long-wave elastic anisotropy produced by horizontal layering, J. Geophys. Res. 67 (1962) 4427–4440.
[5] J.M. Carcione, Anisotropic Q and velocity dispersion of finely layered media, Geophys. Prospect. 40 (1992) 761–783.
[6] J.M. Carcione, Wave Fields in Real Media: Wave Propagation in Anisotropic, Anelastic, Porous and Electromagnetic Media, second ed., in: Handbook of Geophysical Exploration, vol. 38, Elsevier, 2007, revised and extended.
[7] S. Picotti, J.M. Carcione, J.E. Santos, D. Gei, Q-anisotropy in finely-layered media, Geophys. Res. Lett. 37 (2010) L06302. http://dx.doi.org/10.1029/2009GL042046.
[8] J.E. White, Computed seismic speeds and attenuation in rocks with partial gas saturation, Geophysics 40 (1975) 224–232.
[9] G. Mavko, T. Mukerji, J. Dvorkin, The Rock Physics Handbook: Tools for Seismic Analysis in Porous Media, Cambridge Univ. Press, 1998.
[10] J. Douglas Jr., J.E. Santos, D. Sheen, Approximation of scalar waves in the space-frequency domain, Math. Models Methods Appl. Sci. 4 (1994) 509–531.
[11] J. Douglas Jr., J.E. Santos, D. Sheen, X. Ye, Nonconforming Galerkin methods based on quadrilateral elements for second order elliptic problems, Math. Model. Numer. Anal. 33 (1999) 747–770.
[12] P.M. Gauzellino, J.E. Santos, D. Sheen, Frequency domain wave propagation modelling in exploration seismology, J. Comput. Acoust. 9 (2001) 941–955.
[13] J.E. Santos, C.L. Ravazzoli, P.M. Gauzellino, J.M. Carcione, F. Cavallini, Simulation of waves in poro-viscoelastic rocks Saturated by immiscible fluids. Numerical evidence of a second slow wave, J. Comput. Acoust. 12 (2004) 1–21.
[14] J.M. Carcione, H.B. Helle, N.H. Pham, White's model for wave propagation in partially saturated rocks: comparison with poroelastic numerical experiments, Geophysics 68 (2003) 1389–1398.
[15] A.E. Love, A Treatise on the Mathematical Theory of Elasticity, Dover Publications Inc, 1994.
[16] O.M. Lovera, J.E. Santos, Numerical methods for a model for wave propagation in composite anisotropic media, Math. Modelling Numer. Anal. 22 (1988) 159–176.
[17] T. Ha, J.E. Santos, D. Sheen, Nonconforming finite element methods for the simulation of waves in viscoelastic solids, Comput. Methods Appl. Mech. Engrg. 191 (49–50) (2002) 5647–5670.
[18] F.I. Zyserman, P.M. Gauzellino, J.E. Santos, Dispersion analysis of a nonconforming finite element method for the Helmholtz and elastodynamic equations, Int. J. Numer. Methods Eng. 58 (2003) 1381–1395.
[19] J. Douglas Jr., F. Pereira, J.E. Santos, A parallelizable approach to the simulation of waves in dispersive media, in: Mathematical and Numerical Aspects of Wave Propagation (Mandelieu-La Napoule), SIAM, Philadelphia, PA, 1995, pp. 673–682.
[20] P.M. Gauzellino, F.I. Zyserman, J.E. Santos, Nonconforming finite element methods for the three dimensional Helmholtz equation: iterative domain decomposition or global solution? J. Comput. Acoust. 17 (2) (2009) 159–173.